

Bistability in the Unstable Flow of Polymer Solutions Through Porous Media

Christopher A. Browne¹, Audrey Shih¹, and Sujit S. Datta^{1†}

¹Department of Chemical and Biological Engineering, Princeton University,
Princeton, NJ 08544, USA

(Received xx; revised xx; accepted xx)

Polymer solutions are often injected in porous media for applications such as oil recovery and groundwater remediation. As the fluid navigates the tortuous pore space, elastic stresses build up, causing the flow to become unstable at sufficiently large injection rates. However, it is poorly understood how the spatial and temporal characteristics of this unstable flow depend on pore space geometry. We elucidate this dependence by systematically varying the spacing between pore constrictions in a model porous medium. We find that when the pore spacing is large, unstable eddies form upstream of each pore, similar to observations of an isolated pore. By contrast, when the pore spacing is sufficiently small, the flow exhibits a surprising bistability, stochastically switching between two distinct unstable flow states. We hypothesize that this unusual behavior arises from the interplay between flow-induced polymer elongation and relaxation of polymers as they are advected through the porous medium. Consistent with this idea, we find that the flow state in a given pore persists for long times. Moreover, we find that the flow state is correlated between neighboring pores; however, these correlations do not persist long-range. Our results thus help to elucidate the rich array of flow behaviors that can arise in polymer solution flow through porous media.

Key words: Polymers; Viscoelasticity; Porous media.

This preprint was initially submitted on August 6, 2019. An updated version is currently in press at the Journal of Fluid Mechanics and will be posted on arxiv in six months.

1. Introduction

Concentrated polymer solutions have elastic properties that can dramatically alter their flow behavior. Such effects are often harnessed to improve oil recovery and groundwater remediation efforts (Sorbie 2013; Roote 1998). In these cases, an injected polymer solution flows through a tortuous porous medium, such as a reservoir rock or a subsurface aquifer, and displaces trapped non-aqueous fluids from the pore space, enabling them to be recovered downstream. It is therefore critical to be able to predict how the flow behavior depends on the solution properties, injection conditions, and porous medium geometry. Laboratory and field tests provide key empirical measurements of macroscopic variables including fluid pressure and total recovery (Sandiford *et al.* 1964; Durst *et al.* 1981; Pitts *et al.* 1995; Wang *et al.* 2011; Wei *et al.* 2014; Vermolen *et al.* 2014). However, broad

† Email address for correspondence: ssdatta@princeton.edu

application is still limited by an incomplete understanding of the pore-scale features of the fluid flow. As a result, the mechanisms underlying polymer solution-enhanced fluid recovery are still widely debated (Haward & Odell 2003; Odell & Haward 2006; Huh *et al.* 2008; Zaitoun *et al.* 1988, 1998; Clarke *et al.* 2016), and general principles for predicting and controlling the flow are lacking.

Studies of flow in model microfluidic devices provide valuable insights into the pore-scale flow field. Extensive work has focused on the simplified cases of flow into a single pore constriction or flow into narrow constrictions around a single pillar. In these geometries, the polymer chains are aligned and elongated by the flow, generating upstream recirculating eddies that minimize the extensional stress associated with chain misalignment (Batchelor 1971; Boger 1987; Mongruel & Cloitre 1995, 2003; Rodd *et al.* 2007). Polymer elongation along the curved fluid streamlines also produces normal elastic stresses, which persist for a duration λ before relaxing. Thus, at sufficiently large flow speeds, these stresses build up in the solution, further perturbing the flow and causing an elastic instability to arise: an unsteady flow state develops in which the eddies have a broad spectrum of spatial and temporal fluctuations (Koelling & Prud’homme 1991; Lanzaro & Yuan 2011; Kenney *et al.* 2013; Ribeiro *et al.* 2014; Lanzaro *et al.* 2015; Gulati *et al.* 2015; Shi *et al.* 2015; Shi & Christopher 2016; Lanzaro *et al.* 2017; Haward *et al.* 2018; Qin *et al.* 2019). A similar instability also arises in other flows with highly-curved fluid streamlines (Pearson 1976; Larson 1992; Pakdel & McKinley 1996; McKinley *et al.* 1996; Groisman & Steinberg 2000; Pan *et al.* 2013; Galindo-Rosales *et al.* 2014; Sousa *et al.* 2015; Haward *et al.* 2016; Qin & Arratia 2017). However, it is unclear how these effects manifest in a porous medium composed of many successive pore constrictions and expansions, known as throats and bodies respectively.

Imaging of flow through one-dimensional (1D) arrays of *widely-spaced* pores consistently demonstrates the formation of unstable eddies upstream of each pore, similar to the case of an isolated constriction (Galindo-Rosales *et al.* 2012; Khomami & Moreno 1997; Arora *et al.* 2002; Kenney *et al.* 2013; Shi *et al.* 2015; Varshney & Steinberg 2017). By contrast, when the spacing between pores is small, chain elongation may persist across multiple pores as the polymers are advected through the pore space. Thus, memory of strain in one pore may influence the flow in a pore further downstream, potentially providing new spatio-temporal structure to the flow. However, this possibility remains to be explored. Studies conducted at a Reynolds number $Re \sim 20$ and an Elasticity number $El \sim 1$, and thus also subject to inertial effects, show that decreasing the spacing between pores produces stronger flow fluctuations (Shi & Christopher 2016)—providing a clue that polymer memory may indeed influence the flow. Nevertheless, whether and how polymer memory impacts flow through a porous medium has not been fully resolved for the case of $Re \ll 1$ and $El \gg 1$, in which elastic effects dominate and inertial effects do not also arise. This flow regime is particularly relevant to key applications including oil recovery and groundwater remediation, which can have Re ranging from $\sim 10^{-11}$ to 10^{-3} and El ranging from $\sim 10^2$ to 10^{11} .

Here, we use confocal microscopy to investigate the unstable flow of an elastic polymer solution through model porous media at $Re \ll 1$ and $El \gg 1$. The media are made of 1D arrays of pore throats, enabling us to directly test the relative importance of polymer memory on the flow by varying the spacing between pore throats. When the pore spacing is large, unstable eddies form upstream of each pore throat, similar to observations of an isolated pore. By contrast, when the pore spacing is sufficiently small, the flow exhibits a surprising bistability. In each pore, the flow persists over long durations in one of two distinct flow states: an eddy-dominated state in which a pair of large unstable eddies forms in the corners of the pore body, and an eddy-free state in which

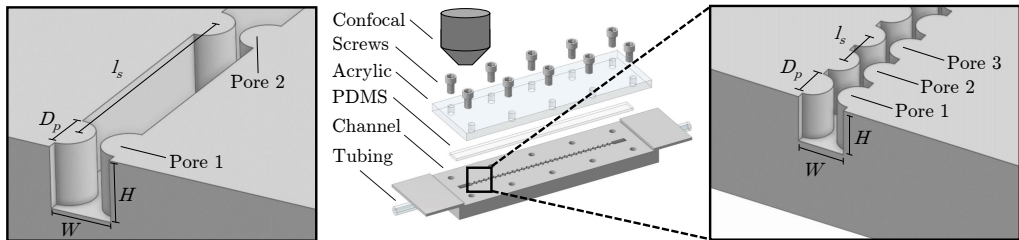


FIGURE 1. Experimental setup. Fluidic channel contains pore throat constrictions defined by opposing hemi-cylindrical posts and is fabricated using a stereolithographic 3D-printer. Dimensions are $W = 2$ mm, $H = 2$ mm, $D_p = 1.6$ mm. We vary the pore throat separation distance l_s and the number of throats in the channel (two examples are shown in the left and right panels). The channel is screwed shut with an acrylic plate over a thin strip of PDMS. Inlet and outlet tubing is glued into 3D-printed holes. The setup is inverted and videos are captured on a confocal microscope; middle panel is vertically flipped for clarity.

strongly-fluctuating fluid pathlines fill the entire pore body and eddies do not form. We hypothesize that this unusual behavior arises from the interplay between flow-induced polymer elongation, which promotes eddy formation, and relaxation of polymers as they are advected between pores, which enables the eddy-free state to form. Consistent with this idea, we find that the flow state in a given pore persists for long times. In addition, we find that the instantaneous flow state is correlated between neighboring pores; however, these correlations do not persist long-range. Our results thus help to elucidate the rich array of behaviors that can arise for polymer solution flow through porous media.

2. Materials and Methods

The void space of a porous medium is typically composed of successive expansions known as pore bodies connected by narrower constrictions known as pore throats (Doyen 1988; Kwiecien *et al.* 1990; Bernabe 1991; Ioannidis & Chatzis 1993). We use 3D printing to make model porous media that recapitulate these geometric features (O’Connell *et al.* 2019). Importantly, this approach provides precise control over the pore space geometry, and yields devices that can be optically interrogated while also withstanding the high pressures that arise during elastic polymer solution flow.

The media are made of straight, square channels having constrictions defined by evenly-spaced hemi-cylindrical posts, as illustrated in Figure 1. Each channel is $W = 2$ mm wide, $H = 2$ mm high, and 7 cm long, with opposing posts of diameter $D_p = 1.6$ mm that are laterally separated by 0.4 mm and spaced by a center-to-center distance of l_s along the flow direction. The space between hemi-cylinders along the flow direction thus defines the pore bodies, while the lateral constriction between opposing hemi-cylinders defines the pore throats. Varying l_s provides a way to systematically test the influence of pore spacing on the flow; hence, our experiments probe an isolated pore throat with $l_s \rightarrow \infty$, a pair of throats with $l_s = 16W$, and an array of thirty throats with $l_s = 1W$.

To fabricate each device, we 3D-print the open-faced channel with a FormLabs Form 2 stereolithography printer, using a proprietary clear polymeric resin (FLGPCL04) composed of methacrylate oligomers and photoinitiators. We then glue inlet and outlet tubing directly into 3D-printed connectors designed to minimize perturbation of the polymers away from the pores. Finally, as shown in figure 1, the whole assembly is screwed shut using a clear acrylic sheet laser-cut to size and placed on top of a thin strip of polydimethylsiloxane (PDMS), which provides a water-tight seal.

The fluid used is an aqueous solution of 18 MDa partially hydrolyzed polyacrylamide

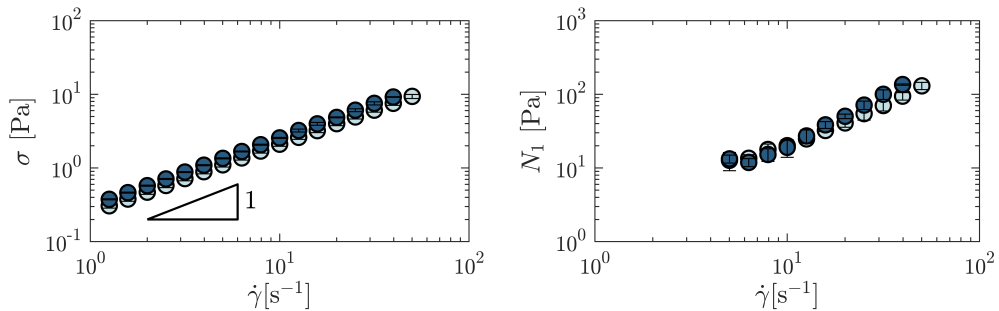


FIGURE 2. Rheology of HPAM polymer solutions. Left panel shows the shear stress σ and right panel shows the first normal stress difference N_1 as functions of the shear rate $\dot{\gamma}$ for the sample used for figures 4c, 6, 7, and 8b–d. Data are taken before (dark blue) and after (light blue) a porous media flow experiment, showing that polymers are not appreciably degraded by the unstable flow. Error bars represent standard deviation over five replicate rheological measurements. Fresh polymer solutions are prepared for each experiment, and all dimensionless quantities described in the text are calculated using rheology on fresh samples.

(HPAM, 30% carboxylated monomers; Polysciences), a polymer commonly used in oil recovery (Sandiford *et al.* 1964; Wei *et al.* 2014). We dissolve 300 ppm HPAM, which corresponds to ≈ 0.3 the overlap concentration, in a solvent of 10 vol% ultrapure water (Millipore) and 90 vol% glycerol (Sigma Aldrich) containing 1 wt% NaCl (Sigma Aldrich). We also seed the polymer solution with 1 ppm of fluorescent 1 μm polystyrene tracer particles (Invitrogen) to enable flow visualization. For each porous medium geometry tested, we prepare a fresh solution and use it within one month.

To visualize the flow, we invert and mount each assembled device on a Nikon A1R inverted laser-scanning confocal microscope. The polymer solution is subsequently injected through the porous medium at a fixed volumetric flow rate Q using a syringe pump (Harvard Apparatus PHD 2000). The time required to inject a single pore throat volume is then given by $\tau_{\text{pv}} \equiv V_{\text{pv}}/Q$, where we define the pore throat volume as the void volume between the beginning and end of a pair of opposing hemi-cylinders, $V_{\text{pv}} = D_p W H - \pi D_p^2 H/4$. In our experiments at sufficiently large Q , we find that unstable fluctuations begin after $\approx 10\tau_{\text{pv}}$ and continue to develop over a time scale of $\approx 40\tau_{\text{pv}}$, after which it reaches a dynamic equilibrium in which the statistical properties of the flow, described in Section 3, do not appreciably change. Our flow visualization measurements are thus taken $\approx 300\tau_{\text{pv}}$ after initiating the flow to ensure that the unstable state is fully developed. We acquire fluorescence images every 33 ms from an optical slice of 17.9 μm thickness in the center of the channel height. To visualize the pathlines of individual tracer particles, we average successive frames for $10\tau_{\text{pv}}$.

We characterize the solution rheology using an Anton Paar MCR-501 rheometer with a 50 mm 1° cone-plate geometry. Figure 2 shows the measured shear stress σ and first normal stress difference N_1 over different shear rates $\dot{\gamma}$ for a representative solution. Furthermore, to assess possible degradation of polymers due to unstable flow in the porous media (Vanapalli *et al.* 2006), we also measure the solution rheology after performing flow experiments at the highest flow rates tested. We find no significant difference between the solution rheology measured before (dark blue points in figure 2) and after (light blue points) flow experiments, indicating minimal polymer degradation due to the unstable flow. For each solution used in each experiment, we obtain at least five replicate measurements of the fluid rheology and use the averaged values in all subsequent calculations.

The shear rate varies approximately linearly with shear rate, with a shear thinning exponent $n \approx 0.92$, indicating that shear thinning effects are small due to the high viscosity of the background solvent. Indeed, the pure solvent viscosity is approximately 0.8 times the measured solution viscosity. However, for accuracy, we use the rate-dependent shear viscosity $\mu(\dot{\gamma}) \equiv \sigma(\dot{\gamma})/\dot{\gamma}$ in all calculations. To determine the shear rate that characterizes flow in porous media, we calculate the wall shear rate in the pore throat at each value of Q tested. We do this using the flow profile for a non-Newtonian fluid having the measured shear-thinning exponent $n = 0.92$, as calculated by Harnett & Irvine (1979) and by Son (2007).

We define the Reynolds number comparing inertial to viscous stresses as $\text{Re} \equiv \rho U_t L / \mu(\dot{\gamma})$, where ρ is the density of the solvent, $U_t \equiv Q/A_t$ is the speed corresponding to flow through the pore throat cross-section $A_t = (W - D_p)H$, and the length scale L is chosen to be half the constriction width $\frac{1}{2}(W - D_p)$. This estimate represents an upper bound for the Reynolds number characterizing the flow; in our porous media experiments, Re ranges from $\approx 8 \times 10^{-5}$ to 7×10^{-3} , indicating that viscous stresses dominate over inertial stresses.

Another common descriptor of elastic flows is the Weissenberg number, which compares elastic stresses to viscous stresses. We define this parameter as $\text{Wi} \equiv N_1(\dot{\gamma})/2\sigma(\dot{\gamma})$, following convention. In our porous media experiments, Wi ranges from ≈ 2 to 9, indicating that elastic stresses dominate. Moreover, the corresponding values of the Elasticity number $\text{El} \equiv \text{Wi}/\text{Re}$, which compares elastic stresses to inertial stresses, are $\gtrsim 900$. Our experiments thus probe the elasticity-dominated flow regime.

An elastic instability arises when elastic stresses—characterized by a large value of Wi —persist over a polymer relaxation length scale λU_t exceeding an effective streamline radius of curvature \mathcal{R} . Thus, unstable flow is predicted to arise for sufficiently large values of the parameter $M \equiv \sqrt{2\text{Wi}} \lambda U_t / \mathcal{R}$, as confirmed experimentally for diverse flow geometries (Pakdel & McKinley 1996; McKinley *et al.* 1996; Haward *et al.* 2016; Zilz *et al.* 2012). Indeed, M quantifies the largest destabilizing term in the Navier-Stokes equations for elastic flows (Pakdel & McKinley 1996; McKinley *et al.* 1996); we thus use this parameter to describe the different flow regimes tested in our experiments. To compute this parameter, we use the rheology measurements to calculate the relaxation time $\lambda = \text{Wi}/\dot{\gamma}$, and use an empirical fit previously established by McKinley *et al.* (1996) to calculate the radius of curvature $\mathcal{R} \approx (2/D_p + 32.5/W)^{-1}$. We find $\lambda \approx 0.3$ to 6 s, in good agreement with previous measurements performed on similar solutions (Qin & Arratia 2017). The corresponding values of M range from ≈ 6 to 31 for our experiments studying flow in porous media.

3. Results

3.1. Isolated pore throat

To test the limiting case of widely-spaced pores ($l_s \rightarrow \infty$), we first investigate flow through an isolated pore throat centered in a channel. At low imposed flow rates, and thus at low values of M , the flow is laminar: the fluid pathlines do not cross and do not change in time. We do not observe eddies—instead, the pathlines smoothly converge as they approach the throat and symmetrically diverge as they leave it. However, above a threshold value of $M \approx 19$, we observe the onset of a flow instability: a pair of unstable eddies forms against the channel walls upstream of the pore throat, as exemplified in figures 3a-c (at the pore throat) and d-f (upstream) for $M = 19.4$, 23.9, and 30.5.

Within each eddy, the fluid recirculates with a speed slower than the mean imposed flow

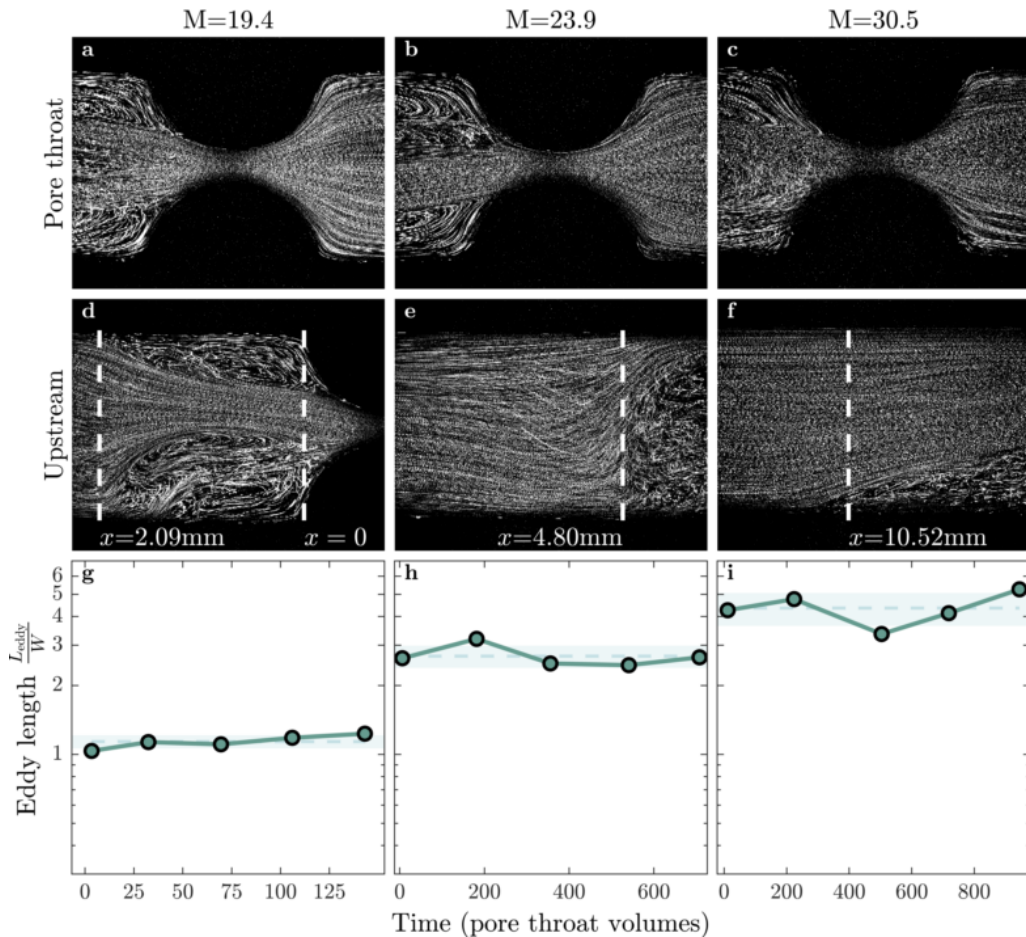


FIGURE 3. Pathline images of polymer solution flow through a straight channel with a single pore throat. Pathline images are averaged over $10\tau_{pv}$. Flow rates are expressed via the M parameter, which equals 19.4, 23.9, and 30.5 for panels **a**, **b**, and **c** respectively, corresponding to Weissenberg numbers $Wi = 5.6$, 6.9 , and 8.8 . **a–c** show strong recirculating eddies upstream of the pore throat, but no downstream eddies at any flow rate. **d–f** show the leftmost edge of the eddies in front of the pore throat. Dashed lines indicate where the eddy-dominated region begins. x indicates the distance in millimeters from the base of the hemi-cylinder. **g–i** show the measured eddy length over time normalized by τ_{pv} . Shaded regions show standard deviation around the temporal mean (dashed lines).

speed in the channel. The fluid pathlines continually fluctuate on long timescales, and also continually cross, indicating that fluctuations in the flow occur on a time scale shorter than the pathline duration of $10\tau_{pv}$ (figures 3d-f). These fluctuations are reflected in the motions of the eddy boundaries and lengths, which also fluctuate as the flow progresses. Similarly, while the fluid in the region formed between the eddies does not recirculate, the fluid pathlines also continually fluctuate on long timescales and continually cross, reflecting the presence of rapid fluctuations in the flow throughout. By contrast, the flow is more steady downstream of the pore throat: we do not observe any eddies or marked temporal changes in the flow for all values of M tested. This result is consistent with the findings of Qin *et al.* (2019), who also found highly unstable eddies upstream of a cylinder

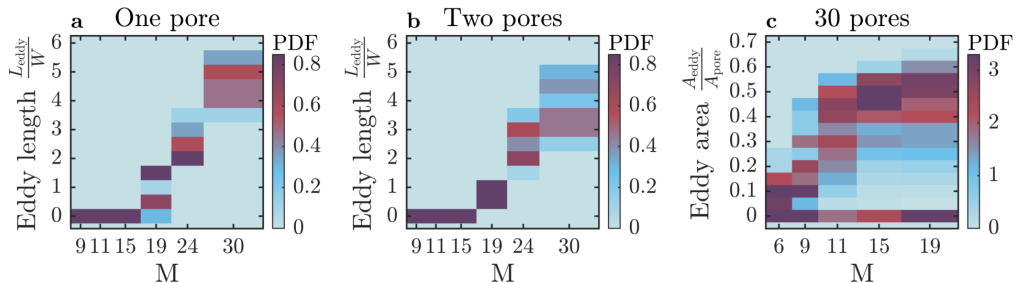


FIGURE 4. Probability density functions of measured eddy sizes for different values of M , averaged over at least $7\tau_{pv}$ and over two separate replicate experiments, displayed vertically as heatmaps. **a** PDFs of L_{eddy}/W for a channel with a single pore throat constriction. For each value of M there is a single characteristic eddy length that increases monotonically with M . **b** PDFs of L_{eddy}/W for a channel with two widely-spaced pores $l_s = 16W$ apart. Again, for each value of M there is a single characteristic eddy length that increases monotonically with M . **c** PDFs of A_{total}/A_{pore} for a porous medium with 30 closely-spaced pores $l_s = W$ apart. Here, the PDFs for $M > 9$ are bimodal, showing multiple characteristic eddy areas (one peak at $\frac{A_{eddy}}{A_{pore}} \approx 60\%$ and one peak at $\frac{A_{eddy}}{A_{pore}} \approx 0$). The two branches in the PDFs indicate a bistability in unstable flow states.

in a channel, but suppressed fluctuations and no eddies downstream. We therefore focus our subsequent analysis on the upstream region.

To further characterize this behavior, we track the eddy length L_{eddy} over time for each value of M tested. We measure L_{eddy} from the base of the hemi-cylinders ($x = 0$ in figure 3d) to the farthest upstream location having a pathline oriented perpendicular to the imposed flow direction (dashed lines in figures 3d-f). Consistent with the visual observations, L_{eddy} fluctuates over time in each experiment, as indicated by the shaded regions in figures 3g-i; however, it fluctuates around a single mean value that increases with M . We quantify these fluctuations using the coefficient of variation c_v , defined as the ratio between the standard deviation and the mean of the measurements of L_{eddy} over time. Taking data from two replicate experiments at these imposed flow rates, we find $c_v \approx 0.3, 0.3$, and 0.4 for $M = 19.4, 23.9$, and 30.5 respectively.

We summarize all of our measurements by plotting the probability density (PDF) of time-averaged measured eddy lengths for each value of M tested. Below the threshold value of $M \approx 19$, we do not observe eddies and hence $L_{eddy} = 0$. By contrast, above this threshold, $L_{eddy} > 0$ fluctuates about a well-defined mean value, which increases with M , as shown in figure 4a. This increase in L_{eddy} is similar to previous measurements for isolated constrictions; these studies demonstrate that eddies form when polymers are elongated, and the size of eddies grows as polymers are increasingly elongated (Batchelor 1971; Boger 1987; Mongruel & Cloitre 1995, 2003; Rodd *et al.* 2007). Our results thus suggest that flow fluctuations arising from unstable flow elongate the individual polymer chains (Sureshkumar *et al.* 1997; Balkovsky *et al.* 2000; Chertkov 2000; Gupta *et al.* 2004; Terrapon *et al.* 2004), which then generate unstable upstream eddies to minimize extensional stresses (Batchelor 1971; Boger 1987; Mongruel & Cloitre 1995, 2003; Rodd *et al.* 2007).

3.2. Two widely-spaced pore throats

We next investigate two pore throats spaced a distance $l_s = 16W$ apart along the flow direction. As we find with an isolated throat, the flow is laminar at low values of M , while above a similar threshold value of $M \approx 19$, we observe the onset of the flow instability.

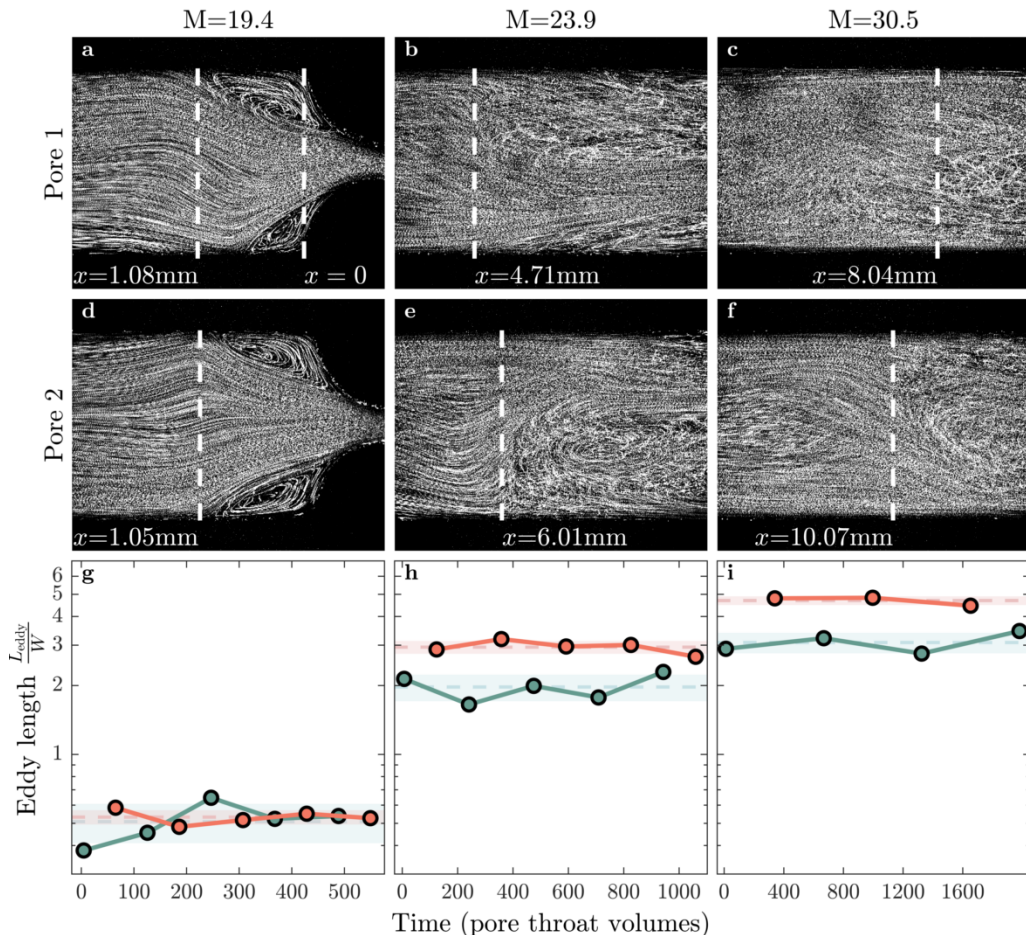


FIGURE 5. Pathline images of polymer solution flow through a straight channel with two pore throats separated by $l_s = 16W$. Pathline images are averaged over $10\tau_{\text{pv}}$. Flow rates are expressed via the M parameter, which equals 19.4, 23.9, and 30.5 for **a**, **b**, and **c** respectively, corresponding to $Wi = 5.6$, 6.9, and 8.8. **a–c** show the leftmost edge of the eddies in front of the first pore throat. **d–f** show the leftmost edge of the eddies in front of the second pore throat. No eddies are observed downstream of either throat. **g–i** show the measured eddy lengths over time normalized by τ_{pv} for pore 1 (green) and pore 2 (red). Shaded regions show standard deviation around the temporal mean (dashed lines).

A pair of unstable eddies again forms against the channel walls upstream of each pore throat, as exemplified in figures 5a–c (first throat) and d–f (second throat). Moreover, as with the isolated pore throat, the flow is more steady immediately downstream of each throat, with no observable eddies or temporal changes in the flow for any values of M tested.

We again quantify this behavior by measuring L_{eddy} over time for each value of M tested. For each pore throat, L_{eddy} again fluctuates around a single mean value that increases with M (figures 5g–i)—similar to the case of an isolated throat. The PDFs of the combined time-averaged measurements of L_{eddy} also reflect its increase with M , as shown in figure 4b. Intriguingly, however, we observe two key differences from the isolated throat. First, while the mean values of L_{eddy} are similar for the two pore throats, eddies upstream of the second throat (red points, figures 5g–i) are slightly larger than

eddies upstream of the first throat (green points) for large values of M . Second, the eddies upstream of the second throat are less unstable—the temporal fluctuations in L_{eddy} are notably suppressed for the second pore throat for all M above the threshold for unstable flow (compare red to green shaded regions in figures 5g-i). Comparing the coefficients of variation confirms this finding: for the first pair of eddies, $c_v = 0.2 \pm 0.1$ while for the second pair, $c_v = 0.10 \pm 0.02$, which is significantly smaller ($p = 0.02$, one-tailed t -test). Thus, when the spacing between pore throats is reduced, the spatio-temporal characteristics of the flow are altered—presumably because polymer elongation can persist across multiple pores.

3.3. Thirty closely-spaced pore throats

To further test the hypothesis that polymer memory impacts flow behavior, we next investigate flow through a medium with an even smaller spacing between pore throats. Specifically, the flow channel contains thirty pore throats spaced a distance $l_s = W$ apart along the flow direction. In this case, we find that the flow behavior is strikingly different from the larger l_s cases described in Sections 3.1 and 3.2.

One key difference is that the threshold for the onset of the flow instability is dramatically lowered. At low imposed flow rates, and thus at low values of M , the flow is laminar: the fluid pathlines do not cross and do not vary over time. In this regime, a pair of small, symmetric, laminar, recirculating eddies forms in the corners of each pore body due to the small spacing between successive pore expansions and constrictions. Above a threshold value of $M \approx 9$ —considerably smaller than the threshold $M \approx 19$ for the single- and double-throat cases—we observe the onset of unstable flow: the fluid pathlines continually cross and vary over time. Thus, decreasing the spacing between pore throats decreases the threshold value of M required for unstable flow, suggesting that polymer memory strongly impacts the flow behavior.

Even more strikingly, we observe two distinct flow states that can arise in each pore body throughout the medium: an ‘eddy-dominated’ state in which a pair of large unstable eddies forms in the corners of the pore body, and an ‘eddy-free’ state in which strongly-fluctuating fluid pathlines fill the entire pore body and eddies do not form. This surprising bistability is illustrated in figure 6, which shows the pathline images taken sequentially from each pore in the medium at $M = 11.4$. Pore 6 exemplifies the eddy-dominated state, with eddies that continually fluctuate both internally and at their boundaries, while pore 2 exemplifies the eddy-free state, with strongly-fluctuating pathlines that fill the entire pore body. Though these snapshots are taken at an optical slice in the center of the channel height, imaging at other heights shows similar flow pathlines, indicating that the spatial structure of the flow does not vary appreciably across the channel height. This observation of distinct pore-scale flow states is in stark contrast to the typical assumption that the spatio-temporal characteristics of unstable flow do not vary through a porous medium: typically no differentiation is made between the flow behaviors that manifest in the different pores.

To quantify this behavior, we measure the two-dimensional (2D) area of the individual eddies A_{eddy} over time for each value of M tested. In laminar flow, the eddies occupy only $\approx 5\%$ of the total area of a pore, which we define as $A_{\text{pore}} \equiv Wl_s - \pi D_p^2/4$. By contrast, unstable eddies in the eddy-dominated state have values of A_{eddy} that fluctuate strongly in time, and whose mean value can be up to $\approx 30\%$ of A_{pore} , while in the eddy-free state $A_{\text{eddy}} \approx 0$. Intriguingly, while the two flow states are each unstable, the flow behavior in each pore body appears to be bistable, as illustrated in figure 7: a pore will persist in a given unstable flow state for a long duration of time before switching, seemingly randomly, to the other flow state. For example, at $M = 11.4$, the upper eddy in pore 13 and the

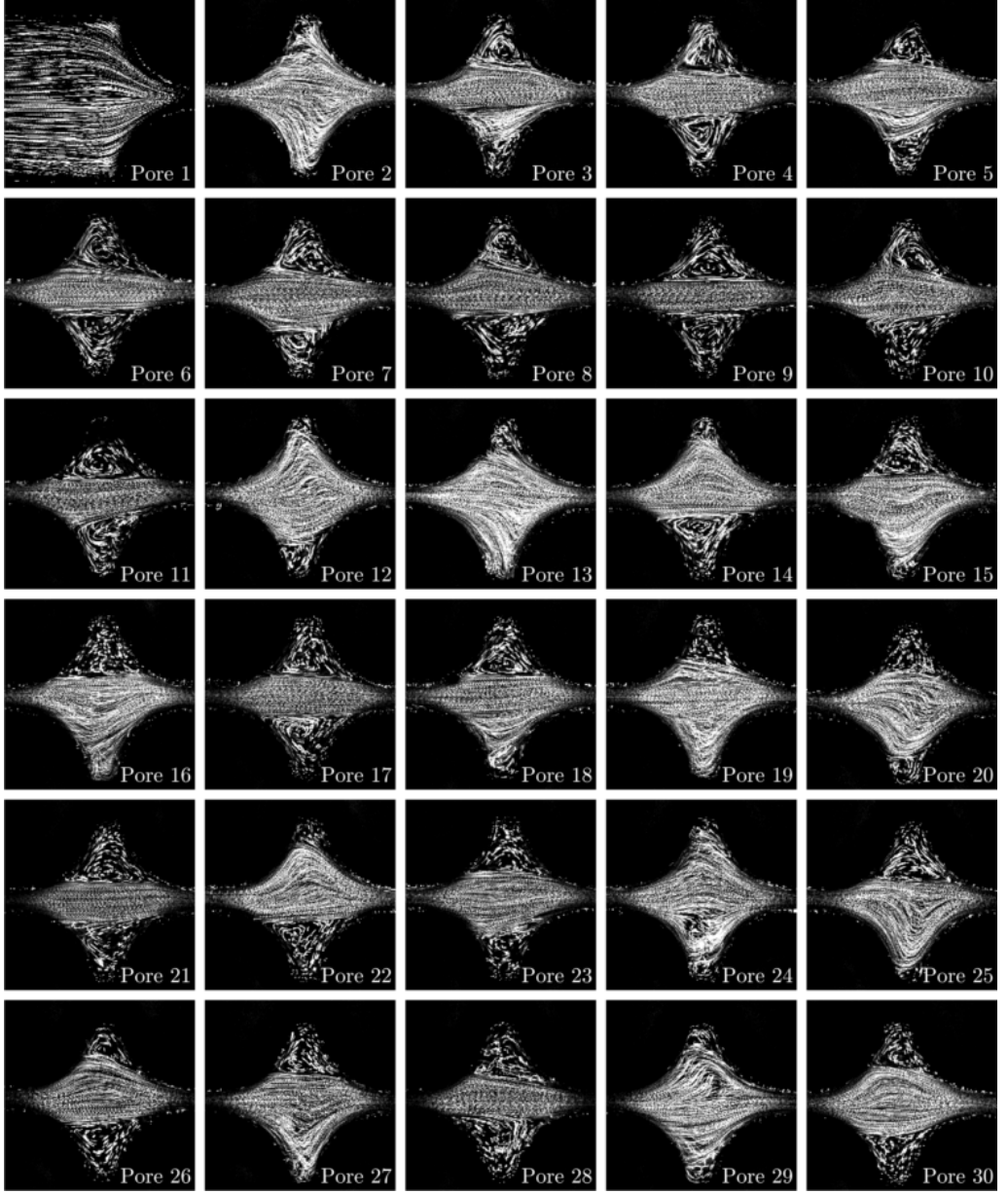


FIGURE 6. Pathline images of polymer solution flow through a porous medium with 30 pore throats separated by $l_s = W = 2$ mm at $M = 11.4$. Images span 2.11 mm across. Pathline images are averaged over $10\tau_{pv}$. Pore 6 exemplifies the eddy-dominated state, with eddies that continually fluctuate both internally and at their boundaries, while pore 2 exemplifies the eddy-free state, with strongly-fluctuating pathlines that fill the entire pore body.

lower eddy in pore 14 (figure 7g, upward-pointing red triangles and downward-pointing green triangles respectively) persist in the eddy-dominated state over the entire imaging duration, while the lower eddy in pore 13 persists in the eddy-free state (downward red triangles). However, the upper eddy in pore 14 initially switches from the eddy-free to the eddy-dominated state, in which it persists for $15\tau_{pv}$ before switching back to the

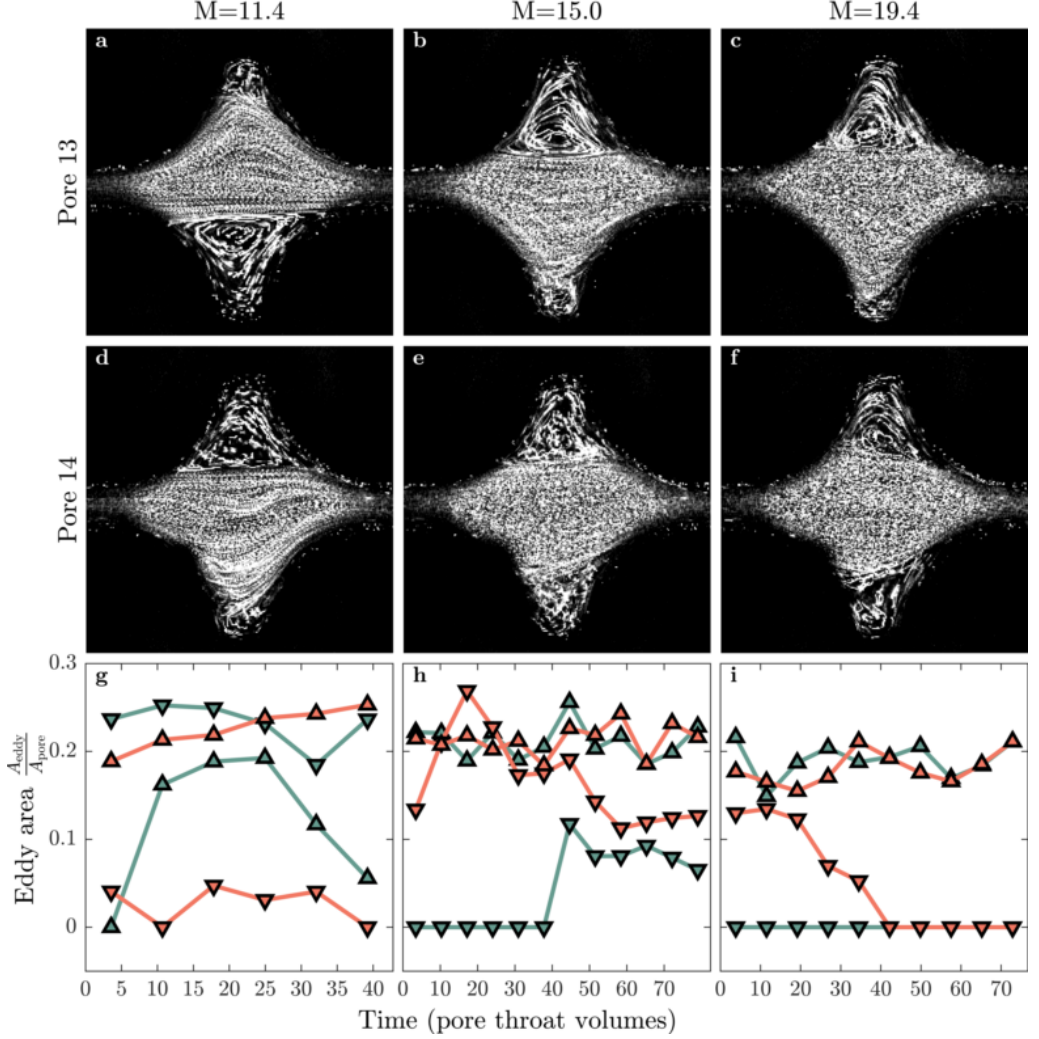


FIGURE 7. Pathline images of polymer solution flow through pores 13 **a–c** and 14 **d–f** at different flow rates corresponding to $M = 11.4$, 15, and 19.4 (left to right). Pathline images are averaged over $10\tau_{\text{pv}}$. **g–i** show the measured eddy areas $A_{\text{eddy}}/A_{\text{pore}}$ over time normalized by τ_{pv} for pore 13 (green) and pore 14 (red). Upward triangles are for the top region of the pore body, downward triangles are for the bottom region of the pore body.

eddy-free state (upward green triangles). We observe this flow bistability in all pores of the medium, and at all values of M tested; two more examples for $M = 15$ and 19.4 are shown in figures 7h–i respectively.

To further characterize the flow bistability shown in figures 7g–i, we plot the PDFs of the time-averaged measurements of A_{total} , which describes the total A_{eddy} measured in each pore combined for all thirty pores in the medium. Below $M \approx 9$, $A_{\text{total}} \approx 10\%$ of A_{pore} , and eddies do not change in time; by contrast, above the onset of the flow instability at $M \approx 9$, the PDFs become bimodal, reflecting the bistability in flow behavior (figure 4c). The eddy-dominated state is represented by the upper branch of the PDFs, in which A_{total} increases with M , eventually plateauing at $\approx 60\%$ of A_{pore} at the highest values of M tested. The eddy-free state is represented by the lower branch of the PDFs, in which

$A_{\text{total}} \approx 0$ over all M . This bistability does not arise in porous media with wider pore spacings: the lower branch of the PDFs does not appear in figures 4a-b. Thus, when the spacing between pore throats is reduced from $l_s = 16W$ to $l_s = W$ —and thus, elongation of individual polymers is more likely to persist across multiple pores—the flow abruptly becomes bistable, exhibiting two coexisting unstable flow states. Indeed, previous work has theorized that unstable flow may bifurcate into two coexisting flow states (Avgousti & Beris 1993; Sureshkumar *et al.* 1994; Varshney & Steinberg 2017); to our knowledge, our work is the first experimental confirmation of this prediction.

3.3.1. Bistability and polymer conformations in flow

How does this unusual flow bistability arise? Previous measurements of polymer conformations indicate that differing fractions of coiled and elongated chains coexist in extensional and unstable flows depending on the imposed flow conditions (Schroeder *et al.* 2003; Gerashchenko *et al.* 2005; François *et al.* 2009). Furthermore, simulations indicate that polymers having different elongation can have dramatically differing pore-scale flow behaviors (Pilitis & Beris 1989, 1991). Thus, we hypothesize that flow bistability arises from the interplay between flow-induced polymer elongation, which promotes eddy formation, and relaxation of polymers as they are advected between pores, which enables the eddy-free state to form.

We first consider a pore in the eddy-dominated state. Polymers entering the pore are likely in an elongated conformation due to the combined influence of unstable flow fluctuations and extension by flow converging into the upstream pore throat. Indeed, previous work has demonstrated that eddies form upstream of a constriction when polymers are elongated (Batchelor 1971; Boger 1987; Mongruel & Cloitre 1995, 2003; Rodd *et al.* 2007). Eddy formation minimizes extensional stresses in the center of the pore: the net flow through the pore body occurs in a nearly-straight channel spanning one pore throat to the next, as can be seen in the example of pore 6 in figure 6. For simplicity, we consider the limit of large M , in which eddies completely fill the corners of the pore body. With the exception of unstable fluctuations, the flow velocities in this channel are then aligned along the flow direction with speed $\sim U_t \equiv Q/A_t \sim 1$ mm/s, and therefore the extensional component of the flow in the channel is minimal. The elongated polymers thus continue to relax as they are advected through this channel, reaching their equilibrium coiled conformation after a duration $\sim \lambda_{\text{rel}}$, the chain relaxation time. We compare this time scale to the residence time required for the polymers to transit across the pore body from the upstream throat to the downstream throat, $\sim l_s/U_t$, yielding an advective Deborah number $\text{De}_{\text{adv}} \equiv \lambda_{\text{rel}}U_t/l_s$. When l_s is small and $\text{De}_{\text{adv}} \gtrsim 1$, chains are still elongated as they enter the next pore body, thereby promoting eddy formation in the current pore and the downstream pore as well. For our experiments in the unstable regime with $l_s = W$, De_{adv} ranges from ~ 0.5 to 3 using $\lambda_{\text{rel}} \sim \lambda \approx 1$ s; this estimate likely under-estimates De_{adv} , since λ_{rel} is known to increase considerably in extensional flow (Clasen *et al.* 2006). Thus, we expect the eddy-dominated state to persist in the pore body over time before random flow fluctuations cause it to switch to the eddy-free state, consistent with our measurements shown in figures 7g-i. We also expect the eddy-dominated state to be correlated between neighboring pores.

We next consider the formation of the eddy-free state. As polymers pass through eddy-dominated pores, they gradually relax to the coiled conformation. When a sufficient fraction of coiled polymers are at the entrance to a pore, there will be no driving force for eddy formation. The pore will thus be in the eddy-free state. The fluid streamlines then diverge from the upstream pore throat, creating a compressional flow that further promotes the coiled conformation. As the polymers continue to traverse the pore body,

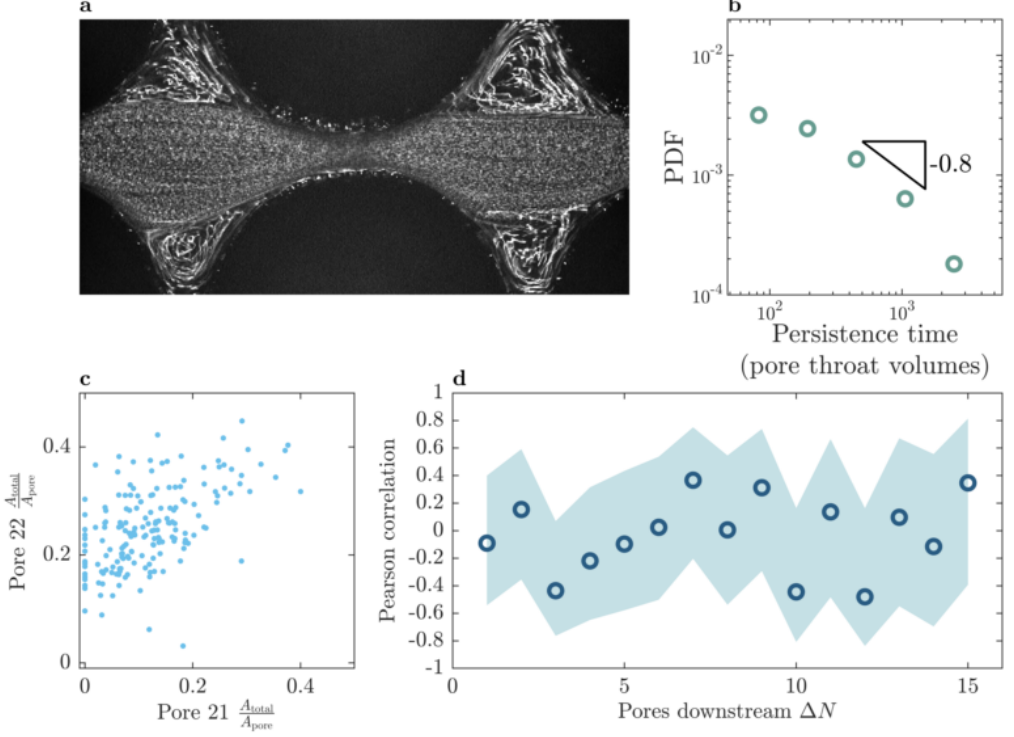


FIGURE 8. **a** Simultaneous pathline imaging of pores 21 and 22 averaged over $10\tau_{\text{pv}}$. Both pores are in the eddy-dominated state. **b** Probability density function of times between discrete switching events, representing the duration over which a given flow state persists, taken up to $2500\tau_{\text{pv}}$. The distribution has a long tail, consistent with a power law that decays as ≈ -0.8 . **c** Instantaneous eddy areas of pore 21 and pore 22 are positively correlated, indicating that flow states are correlated between neighboring pores. **d** Pearson correlation coefficients between pores separated by a length $l_s\Delta N$ and imaged a time $80\tau_{\text{pv}}\Delta N$ apart for $M = 15.0$. The flow state of each pore is averaged over $80\tau_{\text{pv}}$. Light blue shaded region indicates 99% confidence interval for estimated correlation coefficient given the sampling size.

they remain coiled until they encounter the converging flow into the downstream pore throat. This extensional flow partially elongates the chains, which requires a time scale $\sim \lambda_{\text{ret}}$. We again compare this time scale to the residence time required for the polymers to transit from the beginning of the converging region to the downstream throat, in this case $\sim H(WD_p/2 - \pi D_p^2/8)/Q$. This comparison yields another advective Deborah number $\text{De}'_{\text{adv}} \equiv \lambda_{\text{ret}}Q/[H(WD_p/2 - \pi D_p^2/8)]$. When $\text{De}'_{\text{adv}} \gtrsim 1$, chains are not elongated as they enter the next pore body, thereby promoting the eddy-free state in the current pore and the downstream pore as well. For our experiments in the unstable regime, De'_{adv} ranges from ≈ 0.7 to 5 using $\lambda_{\text{ret}} \sim \lambda \approx 1$ s, although these values again likely underestimate De'_{adv} . Thus, similar to the eddy-dominated state, we expect the eddy-free state to persist in the pore body over time before random flow fluctuations cause it to switch to the eddy-free state, consistent with our measurements shown in figures 7g-i. Moreover, we again expect the eddy-free state to be correlated between neighboring pores.

3.3.2. Temporal and Spatial Characteristics of the Flow

The hypothesis presented in Section 3.3.1 makes two testable predictions: first, that the two different unstable flow states each persist over long times before randomly switching,

and second, that the flow states between neighboring pores are correlated. We test these predictions by investigating the temporal and spatial characteristics of the pore-scale flow. Specifically, we simultaneously image two neighboring pores within the medium (pores 21 and 22) and monitor their flow states for $2500\tau_{pv}$. Figure 8a shows a snapshot of the flow pathlines imaged within both pores simultaneously at an instance when both pores are in the eddy-dominated state.

The data in figures 7g–i support the first prediction that the two distinct flow states persist over long times. To further test this prediction, we measure the distribution of durations over which each flow state persists in a given pore before switching to the other state; we define a switching event as the instant when the total eddy area A_{total} in a given pore crosses a threshold value of $0.15 A_{pore}$. This threshold is motivated by the clear separation between the eddy-dominated and eddy-free states indicated by the probability density functions in figure 4c. In agreement with our expectation, we find a broad distribution of long flow persistence times, as shown in figure 8b. Intriguingly, the decay of the measured probability density function is consistent with a power law of exponent ≈ -0.8 ; thus, unstable flow does not appear to have a characteristic persistence time, and instead can persist for longer than $2500\tau_{pv}$, confirming our first prediction.

The image in figure 8a supports the second prediction that the flow states in neighboring pores are correlated. To further test this prediction, we measure the instantaneous total eddy area A_{total} in both pores 21 and 22. These measurements, spanning several thousand τ_{pv} , are shown in figure 8c. We find that A_{total} for pore 22 is positively correlated with A_{total} for pore 21; the Pearson correlation coefficient is $\rho_{A_{21}, A_{22}} = 0.55$, confirming a positive correlation between both quantities that is statistically significant ($p < 0.001$, two-tailed t -test). Thus, the unstable flow states in neighboring pores are correlated with each other, confirming our second prediction.

However, imaging of flow through the entire medium (figure 6) suggests that these spatial and temporal correlations across neighboring pores are not sufficient to produce long-range correlations in the flow over long time scales. To test whether such long-range correlations persist, we sequentially measure the total eddy areas in each pore, each for $80\tau_{pv}$, throughout the entire medium. We then calculate the Pearson correlation coefficient between the values of A_{total}/A_{pore} measured in pores that are separated by a length $l_s\Delta N$, where ΔN ranges from 1 to 15. We find no long-range correlations in the flow over these long time scales: the Pearson correlation coefficient does not statistically deviate from zero for any values of ΔN throughout the medium, as shown in figure 8d. Thus, while unstable flow states are correlated over long times across neighboring pores, these correlations do not persist throughout the entire medium—presumably due to the influence of random fluctuations in the flow. We note, however, that our data do not preclude the possibility that long-range correlations may arise at shorter time scales; our imaging only probes correlations between pores $l_s\Delta N$ apart that can persist over a time scale exceeding $\approx 80\Delta N\tau_{pv}$. Investigating whether the flow correlations described in figure 8a–c can persist over broader spatial and temporal ranges will be a useful direction for future work.

4. Conclusions

Our work describes the first experimental observations of bistability in the flow of an elastic polymer solution through porous media, confirming previous theoretical predictions (Avgousti & Beris 1993; Sureshkumar *et al.* 1994; Varshney & Steinberg 2017). We find that when the spacing between pores is sufficiently small, and when the imposed flow rate is sufficiently large, the flow stochastically switches between two distinct unstable flow

states. In the eddy-dominated state, a pair of large unstable eddies forms in the corners of a pore body, while in the eddy-free state, strongly-fluctuating fluid pathlines fill the entire pore body and eddies do not form. Our work thus indicates that in a porous medium the pore-scale flow behavior might not be uniquely determined by the M parameter (Pakdel & McKinley 1996; McKinley *et al.* 1996) or the Weissenberg number Wi , as is often assumed. Extending these findings to 2D and 3D media, in which transverse interactions between pores may also play a role (Talwar & Khomami 1995; Khomami & Moreno 1997; Arora *et al.* 2002; Sadanandan & Sureshkumar 2004; Vázquez-Quesada & Ellero 2012; Howe *et al.* 2015; Clarke *et al.* 2016; Kawale *et al.* 2017*b,a*; De *et al.* 2016, 2017*a,b,c*, 2018*a,b*; Walkama *et al.* 2019), will be an important direction for future studies.

We hypothesize that the flow bistability arises from the interplay between flow-induced polymer elongation, which promotes eddy formation, and relaxation of polymers as they are advected between pores, which enables the eddy-free state to form. Consistent with this idea, we find that the eddy sizes increase with the imposed flow rate. Additionally, we find that a flow state in a given pore persists over long time scales before switching to the other flow state, presumably due to random flow fluctuations. Flow state is also strongly correlated between neighboring pores; however, these correlations are not sufficient to produce long-range correlations in the flow through the entire medium over long time scales. Elucidating the factors that determine the length and time scales over which flow correlations persist will be an interesting direction for future work.

Indeed, the different spatial and temporal characteristics of the two flow states could impact fluid mixing and the displacement of trapped immiscible fluids from the pore space in a variety of ways (Babayekhorasani *et al.* 2016; Aramideh *et al.* 2019). Thus, a deeper understanding of the flow behaviors discovered here could provide guidance to applications that require specific mixing or fluid displacement behaviors. Examples include oil recovery and groundwater remediation, in which the viscous forces exerted by the polymer solution could displace a trapped fluid from the pores, or unstable mixing due to the fluid instability could improve the transport of oxidants and surfactants to the fluid interface. Such flow behaviors could also be harnessed in other emerging applications such as controlling mixing in lab-on-a-chip devices.

It is a pleasure to acknowledge P. D. Olmsted, A. Z. Panagiotopoulos, R. K. Prud'homme, B. Qin, and H. A. Stone for stimulating discussions, and the Stone Lab for access to the SLA printer and the rheometer. Acknowledgment is made to the Donors of the American Chemical Society Petroleum Research Fund for partial support of this research. This material is also based upon work supported by the National Science Foundation Graduate Research Fellowship Program (to C.A.B.) under Grant No. DGE-1656466. Any opinions, findings, and conclusions or recommendations expressed in this material are those of the authors and do not necessarily reflect the views of the National Science Foundation. C.A.B. was also supported in part by the Mary and Randall Hack Graduate Award of the Princeton Environmental Institute. A.S. was supported in part by the Lidow Thesis Fund at Princeton University and the Dede T. Bartlett P03 Fund for Student Research through the Andlinger Center for Energy and the Environment.

REFERENCES

- ARAMIDEH, SOROUGH, VLACHOS, PAVLOS P & ARDEKANI, AREZOO M 2019 Nanoparticle dispersion in porous media in viscoelastic polymer solutions. *Journal of Non-Newtonian Fluid Mechanics* **268**, 75–80.
- ARORA, K, SURESHKUMAR, R & KHOMAMI, B 2002 Experimental investigation of purely elastic

- instabilities in periodic flows. *Journal of non-newtonian fluid mechanics* **108** (1-3), 209–226.
- AVGousti, Marios & Beris, Antony N 1993 Non-axisymmetric modes in viscoelastic taylor-couette flow. *Journal of non-newtonian fluid mechanics* **50** (2-3), 225–251.
- BABAYEKHORASANI, FIROOZEH, DUNSTAN, DAVE E, KRISHNAMOORTI, RAMANAN & CONRAD, JACINTA C 2016 Nanoparticle dispersion in disordered porous media with and without polymer additives. *Soft Matter* **12** (26), 5676–5683.
- BALKOVSKY, E, FOUXON, A & LEBEDEV, V 2000 Turbulent dynamics of polymer solutions. *Physical review letters* **84** (20), 4765.
- BATCHELOR, GK 1971 The stress generated in a non-dilute suspension of elongated particles by pure straining motion. *Journal of Fluid Mechanics* **46** (4), 813–829.
- BERNABE, Y. 1991 Pore geometry and pressure dependence of the transport properties in sandstones. *Geophysics* **56** (4), 424–576.
- BOGER, DV 1987 Viscoelastic flows through contractions. *Annual review of fluid mechanics* **19** (1), 157–182.
- CHERTKOV, MICHAEL 2000 Polymer stretching by turbulence. *Physical review letters* **84** (20), 4761.
- CLARKE, ANDREW, HOWE, ANDREW M, MITCHELL, JONATHAN, STANILAND, JOHN, HAWKES, LAURENCE A & OTHERS 2016 How viscoelastic-polymer flooding enhances displacement efficiency. *SPE Journal* **21** (03), 675–687.
- CLASEN, C., PLOG, J. P., KULICKE, W.-M., OWENS, M., MACOSKO, C., SCRIVEN, L. E., VERANI, M. & MCKINLEY, G. H. 2006 How dilute are dilute solutions in extensional flows? *Journal of Rheology* **50**, 849–881.
- DE, S, KOESEN, SP, MAITRI, RV, GOLOMBOK, M, PADDING, JT & VAN SANTVOORT, JFM 2018a Flow of viscoelastic surfactants through porous media. *AIChE Journal* **64** (2), 773–781.
- DE, S, KRISHNAN, P, VAN DER SCHAAF, J, KUIPERS, JAM, PETERS, EAJF & PADDING, JT 2018b Viscoelastic effects on residual oil distribution in flows through pillared microchannels. *Journal of colloid and interface science* **510**, 262–271.
- DE, S, KUIPERS, JAM, PETERS, EAJF & PADDING, JT 2017a Viscoelastic flow simulations in model porous media. *Physical Review Fluids* **2** (5), 053303.
- DE, S, KUIPERS, JAM, PETERS, EAJF & PADDING, JT 2017b Viscoelastic flow simulations in random porous media. *Journal of Non-Newtonian Fluid Mechanics* **248**, 50–61.
- DE, SHAUVIK, KUIPERS, JOHANNES AM, PETERS, ELIAS AJF & PADDING, JOHAN T 2017c Viscoelastic flow past mono-and bidisperse random arrays of cylinders: flow resistance, topology and normal stress distribution. *Soft matter* **13** (48), 9138–9146.
- DE, S, VAN DER SCHAAF, J, DEEN, NG, KUIPERS, JAM, PETERS, EAJF & PADDING, JT 2016 Elastic instabilities in flows through pillared micro channels. *arXiv preprint arXiv:1607.03672* .
- DOYEN, PHILIPPE M. 1988 Permeability, Conductivity, and Pore Geometry of Sandstone. *Journal of Geophysical Research* **93** (B7), 7729–7740.
- DURST, FRBU, HAAS, R & KACZMAR, BU 1981 Flows of dilute hydrolyzed polyacrylamide solutions in porous media under various solvent conditions. *Journal of Applied Polymer Science* **26** (9), 3125–3149.
- FRANÇOIS, NICOLAS, AMAROUCHENE, YACINE, LOUNIS, BRAHIM & KELLAY, HAMID 2009 Polymer conformations and hysteretic stresses in nonstationary flows of polymer solutions. *EPL (Europhysics Letters)* **86** (3), 34002.
- GALINDO-ROSALES, FRANCISCO J, CAMPO-DEAÑO, LAURA, PINHO, FT, VAN BOKHORST, E, HAMERSMA, PJ, OLIVEIRA, MÓNICA SN & ALVES, MA 2012 Microfluidic systems for the analysis of viscoelastic fluid flow phenomena in porous media. *Microfluidics and nanofluidics* **12** (1-4), 485–498.
- GALINDO-ROSALES, FRANCISCO J, CAMPO-DEAÑO, LAURA, SOUSA, PATRÍCIA C, RIBEIRO, VERA M, OLIVEIRA, MÓNICA SN, ALVES, MANUEL A & PINHO, FERNANDO T 2014 Viscoelastic instabilities in micro-scale flows. *Experimental Thermal and Fluid Science* **59**, 128–139.
- GERASHCHENKO, S, CHEVALLARD, C & STEINBERG, V 2005 Single-polymer dynamics: Coil-stretch transition in a random flow. *EPL (Europhysics Letters)* **71** (2), 221.

- GROISMAN, ALEXANDER & STEINBERG, VICTOR 2000 Elastic turbulence in a polymer solution flow. *Nature* **405** (6782), 53.
- GULATI, SHELLY, MULLER, SUSAN J & LIEPMANN, DORIAN 2015 Flow of dna solutions in a microfluidic gradual contraction. *Biomicrofluidics* **9** (5), 054102.
- GUPTA, VK, SURESHKUMAR, R & KHOMAMI, B 2004 Polymer chain dynamics in newtonian and viscoelastic turbulent channel flows. *Physics of Fluids* **16** (5), 1546–1566.
- HARNETT, JAMES P & IRVINE, THOMAS F 1979 *Advances in heat transfer*. Elsevier Science.
- HAWARD, SIMON J, MCKINLEY, GARETH H & SHEN, AMY Q 2016 Elastic instabilities in planar elongational flow of monodisperse polymer solutions. *Scientific reports* **6**, 33029.
- HAWARD, SIMON J & ODELL, JEFFREY A 2003 Viscosity enhancement in non-newtonian flow of dilute polymer solutions through crystallographic porous media. *Rheologica acta* **42** (6), 516–526.
- HAWARD, SIMON J, TODA-PETERS, KAZUMI & SHEN, AMY Q 2018 Steady viscoelastic flow around high-aspect-ratio, low-blockage-ratio microfluidic cylinders. *Journal of Non-Newtonian Fluid Mechanics* **254**, 23–35.
- HOWE, ANDREW M, CLARKE, ANDREW & GIERNALCZYK, DANIEL 2015 Flow of concentrated viscoelastic polymer solutions in porous media: effect of mw and concentration on elastic turbulence onset in various geometries. *Soft Matter* **11** (32), 6419–6431.
- HUH, CHUN, POPE, GARY ARNOLD & OTHERS 2008 Residual oil saturation from polymer floods: laboratory measurements and theoretical interpretation. In *SPE Symposium on Improved Oil Recovery*. Society of Petroleum Engineers.
- IOANNIDIS, MARIOS A. & CHATZIS, IOANNIS 1993 Network modelling of pore structure and transport properties of porous media. *Chemical Engineering Science* **48** (5), 951–972.
- KAWALE, DURGESH, BOUWMAN, GELMER, SACHDEV, SHAURYA, ZITHA, PACELLI LJ, KREUTZER, MICHEL T, ROSSEN, WILLIAM R & BOUKANY, POUYAN E 2017a Polymer conformation during flow in porous media. *Soft matter* **13** (46), 8745–8755.
- KAWALE, DURGESH, MARQUES, ESTEBAN, ZITHA, PACELLI LJ, KREUTZER, MICHEL T, ROSSEN, WILLIAM R & BOUKANY, POUYAN E 2017b Elastic instabilities during the flow of hydrolyzed polyacrylamide solution in porous media: Effect of pore-shape and salt. *Soft matter* **13** (4), 765–775.
- KENNEY, STEPHEN, POPER, KADE, CHAPAGAIN, GANESH & CHRISTOPHER, GORDON F 2013 Large Deborah number flows around confined microfluidic cylinders. *Rheologica Acta* **52** (5), 485–497.
- KHOMAMI, BAMIN & MORENO, LUIS D 1997 Stability of viscoelastic flow around periodic arrays of cylinders. *Rheologica acta* **36** (4), 367–383.
- KOELLING, KW & PRUD'HOMME, ROBERT KRAFFT 1991 Instabilities in multi-hole converging flow of viscoelastic fluids. *Rheologica acta* **30** (6), 511–522.
- KWIECIEN, M. J., MACDONALD, I. F. & DULLIEN, F. A.L. 1990 Three-dimensional reconstruction of porous media from serial section data. *Journal of Microscopy* **159** (3), 343–359.
- LANZARO, ALFREDO, CORBETT, DANIEL & YUAN, XUE-FENG 2017 Non-linear dynamics of semi-dilute paam solutions in a microfluidic 3d cross-slot flow geometry. *Journal of Non-Newtonian Fluid Mechanics* **242**, 57–65.
- LANZARO, ALFREDO, LI, ZHUO & YUAN, XUE-FENG 2015 Quantitative characterization of high molecular weight polymer solutions in microfluidic hyperbolic contraction flow. *Microfluidics and Nanofluidics* **18** (5-6), 819–828.
- LANZARO, ALFREDO & YUAN, XUE-FENG 2011 Effects of contraction ratio on non-linear dynamics of semi-dilute, highly polydisperse paam solutions in microfluidics. *Journal of Non-Newtonian Fluid Mechanics* **166** (17-18), 1064–1075.
- LARSON, RG 1992 Flow-induced mixing, demixing, and phase transitions in polymeric fluids. *Rheologica Acta* **31** (6), 497–520.
- MCKINLEY, GARETH H, PAKDEL, PEYMAN & ÖZTEKIN, ALPARSLAN 1996 Rheological and geometric scaling of purely elastic flow instabilities. *Journal of Non-Newtonian Fluid Mechanics* **67**, 19–47.
- MONGRUEL, A & CLOITRE, M 1995 Extensional flow of semidilute suspensions of rod-like particles through an orifice. *Physics Of Fluids* **7** (11), 2546–2552.
- MONGRUEL, A & CLOITRE, M 2003 Axisymmetric orifice flow for measuring the elongational

- viscosity of semi-rigid polymer solutions. *Journal of non-newtonian fluid mechanics* **110** (1), 27–43.
- O’CONNELL, MARGARET G, LU, NANCY B, BROWNE, CHRISTOPHER A & DATTA, SUJIT S 2019 Cooperative size sorting of deformable particles in porous media. *Soft Matter* **15**, 3620.
- ODELL, JA & HAWARD, SJ 2006 Viscosity enhancement in non-newtonian flow of dilute aqueous polymer solutions through crystallographic and random porous media. *Rheologica acta* **45** (6), 853–863.
- PAKDEL, PEYMAN & MCKINLEY, GARETH H 1996 Elastic instability and curved streamlines. *Physical Review Letters* **77** (12), 2459.
- PAN, L, MOROZOV, A, WAGNER, C & ARRATIA, PE 2013 Nonlinear elastic instability in channel flows at low reynolds numbers. *Physical review letters* **110** (17), 174502.
- PEARSON, JRA 1976 Instability in non-newtonian flow. *Annual Review of Fluid Mechanics* **8** (1), 163–181.
- PILITSIS, STERGIOS & BERIS, ANTONY N 1989 Calculations of steady-state viscoelastic flow in an undulating tube. *Journal of Non-Newtonian Fluid Mechanics* **31** (3), 231–287.
- PILITSIS, STERGIOS & BERIS, ANTONY N 1991 Viscoelastic flow in an undulating tube. part ii. effects of high elasticity, large amplitude of undulation and inertia. *Journal of non-newtonian fluid mechanics* **39** (3), 375–405.
- PITTS, MALCOLM J, CAMPBELL, TOM A, SURKALO, HARRY, WYATT, KON & OTHERS 1995 Polymer flood of the rapdan pool, saskatchewan, canada. *SPE Reservoir Engineering* **10** (03), 183–186.
- QIN, BOYANG & ARRATIA, PAULO E 2017 Characterizing elastic turbulence in channel flows at low reynolds number. *Physical Review Fluids* **2** (8), 083302.
- QIN, BOYANG, SALIPANTE, PAUL F, HUDSON, STEVEN D & ARRATIA, PAULO E 2019 Upstream vortex and elastic wave in the viscoelastic flow around a confined cylinder. *Journal of Fluid Mechanics* **864**.
- RIBEIRO, VM, COELHO, PM, PINHO, FT & ALVES, MA 2014 Viscoelastic fluid flow past a confined cylinder: Three-dimensional effects and stability. *Chemical engineering science* **111**, 364–380.
- RODD, LE, COOPER-WHITE, JJ, BOGER, DV & MCKINLEY, GH 2007 Role of the elasticity number in the entry flow of dilute polymer solutions in micro-fabricated contraction geometries. *Journal of Non-Newtonian Fluid Mechanics* **143** (2-3), 170–191.
- ROOTE, DS 1998 Technology status report: in situ flushing. *Ground Water Remediation Technology Analysis Center (available at <http://www.gwrtac.org>)*.
- SADANANDAN, B & SURESHKUMAR, RADHAKRISHNA 2004 Global linear stability analysis of viscoelastic flow through a periodic channel. *Journal of non-newtonian fluid mechanics* **122** (1-3), 55–67.
- SANDIFORD, BB & OTHERS 1964 Laboratory and field studies of water floods using polymer solutions to increase oil recoveries. *Journal of Petroleum Technology* **16** (08), 917–922.
- SCHROEDER, CHARLES M, BABCOCK, HAZEN P, SHAQFEH, ERIC SG & CHU, STEVEN 2003 Observation of polymer conformation hysteresis in extensional flow. *Science* **301** (5639), 1515–1519.
- SHI, XUEDA & CHRISTOPHER, GORDON F 2016 Growth of viscoelastic instabilities around linear cylinder arrays. *Physics of Fluids* **28** (12), 124102.
- SHI, XUEDA, KENNEY, STEPHEN, CHAPAGAIN, GANESH & CHRISTOPHER, GORDON F 2015 Mechanisms of onset for moderate mach number instabilities of viscoelastic flows around confined cylinders. *Rheologica Acta* **54** (9-10), 805–815.
- SON, YOUNGGON 2007 Determination of shear viscosity and shear rate from pressure drop and flow rate relationship in a rectangular channel. *Polymer* **48** (2), 632–637.
- SORBIE, KENNETH S 2013 *Polymer-improved oil recovery*. Springer Science & Business Media.
- SOSA, PC, PINHO, FT, OLIVEIRA, MSN & ALVES, MA 2015 Purely elastic flow instabilities in microscale cross-slot devices. *Soft matter* **11** (45), 8856–8862.
- SURESHKUMAR, RADHAKRISHNA, BERIS, ANTONY N & AVGOUSTI, MARIOS 1994 Non-axisymmetric subcritical bifurcations in viscoelastic taylor–couette flow. *Proceedings of the Royal Society of London. Series A: Mathematical and Physical Sciences* **447** (1929), 135–153.

- SURESHKUMAR, R, BERIS, ANTONY N & HANDLER, ROBERT A 1997 Direct numerical simulation of the turbulent channel flow of a polymer solution. *Physics of Fluids* **9** (3), 743–755.
- TALWAR, KAPIL K & KHOMAMI, BAMIN 1995 Flow of viscoelastic fluids past periodic square arrays of cylinders: inertial and shear thinning viscosity and elasticity effects. *Journal of Non-Newtonian Fluid Mechanics* **57** (2-3), 177–202.
- TERRAPON, VE, DUBIEF, YVES, MOIN, PARVIZ, SHAQFEH, ERIC SG & LELE, SANJIVA K 2004 Simulated polymer stretch in a turbulent flow using brownian dynamics. *Journal of Fluid Mechanics* **504**, 61–71.
- VANAPALLI, SIVA A, CECCIO, STEVEN L & SOLOMON, MICHAEL J 2006 Universal scaling for polymer chain scission in turbulence. *Proceedings of the National Academy of Sciences* **103** (45), 16660–16665.
- VARSHNEY, ATUL & STEINBERG, VICTOR 2017 Elastic wake instabilities in a creeping flow between two obstacles. *Physical Review Fluids* **2** (5), 051301.
- VÁZQUEZ-QUESADA, A & ELLERO, M 2012 Sph simulations of a viscoelastic flow around a periodic array of cylinders confined in a channel. *Journal of Non-Newtonian Fluid Mechanics* **167**, 1–8.
- VERMOLEN, ECM, VAN HAASTERECHT, MJT, MASALMEH, SK & OTHERS 2014 A systematic study of the polymer visco-elastic effect on residual oil saturation by core flooding. In *SPE EOR Conference at Oil and Gas West Asia*. Society of Petroleum Engineers.
- WALKAMA, DEREK M, WAISBORD, NICOLAS & GUASTO, JEFFREY S 2019 Disorder suppresses chaos in viscoelastic flows. *arXiv preprint arXiv:1906.11868* .
- WANG, DEMIN, WANG, GANG, XIA, HUIFEN & OTHERS 2011 Large scale high visco-elastic fluid flooding in the field achieves high recoveries. In *SPE Enhanced Oil Recovery Conference*. Society of Petroleum Engineers.
- WEI, BING, ROMERO-ZERÓN, LAURA & RODRIGUE, DENIS 2014 Oil displacement mechanisms of viscoelastic polymers in enhanced oil recovery (eor): a review. *Journal of Petroleum Exploration and Production Technology* **4** (2), 113–121.
- ZAITOUN, A, BERTIN, H, LASSEUX, D & OTHERS 1998 Two-phase flow property modifications by polymer adsorption. In *SPE/DOE improved oil recovery symposium*. Society of Petroleum Engineers.
- ZAITOUN, A, KOHLER, N & OTHERS 1988 Two-phase flow through porous media: effect of an adsorbed polymer layer. In *SPE Annual Technical Conference and Exhibition*. Society of Petroleum Engineers.
- ZILZ, J, POOLE, RJ, ALVES, MA, BARTOLO, D, LEVACHÉ, B & LINDNER, A 2012 Geometric scaling of a purely elastic flow instability in serpentine channels. *Journal of Fluid Mechanics* **712**, 203–218.